Monthly Notices
of the
ROYAL ASTRONOMICAL SOCIETY

MNRAS **463,** 449–458 (2016)
Advance Access publication 2016 August 11

doi:10.1093/mnras/stw2003

The *Hubble Space Telescope* UV Legacy Survey of Galactic globular clusters – X. The radial distribution of stellar populations in NGC 2808

M. Simioni,[1,2,3,4★] A. P. Milone,[5] L. R. Bedin,[4] A. Aparicio,[1,2] G. Piotto,[3,4] E. Vesperini[6] and J. Hong[6]

[1]*Instituto de Astrofisica de Canarias, E-38200 La Laguna, Tenerife, Canary Islands, Spain*
[2]*Department of Astrophysics, University of La Laguna, E-38200 La Laguna, Tenerife, Canary Islands, Spain*
[3]*Dipartimento di Fisica e Astronomia 'Galileo Galilei', Università degli Studi di Padova, Vicolo dell'Osservatorio 3, I-35122 Padova, Italy*
[4]*INAF – Osservatorio Astronomico di Padova, Vicolo dell'Osservatorio 5, I-35122 Padova, Italy*
[5]*Research School of Astronomy and Astrophysics, Australian National University, Cotter Road, Weston, ACT 2611, Australia*
[6]*Department of Astronomy, Indiana University, Bloomington, IN 47401, USA*

Accepted 2016 August 7. Received 2016 July 25; in original form 2016 June 7

ABSTRACT

Due to their extreme helium abundance, the multiple stellar populations of the globular cluster NGC 2808 have been widely investigated from a photometric, spectroscopic, and kinematic perspective. The most striking feature of the colour–magnitude diagram of NGC 2808 is the triple main sequence (MS), with the red MS corresponding to a stellar population with primordial helium, and the middle and the blue MS being enhanced in helium up to $Y \sim 0.32$ and $\sim$0.38, respectively. A recent study has revealed that this massive cluster hosts at least five distinct stellar populations (A, B, C, D, and E). Among them populations A, B, and C correspond to the red MS, while populations C and D are connected to the middle and the blue MS. In this paper, we exploit *Hubble Space Telescope* photometry to investigate the radial distribution of the red, the middle, and the blue MS from the cluster centre out to about 8.5 arcmin. Our analysis shows that the radial distribution of each of the three MSs is different. In particular, as predicted from multiple-population formation models, both the blue MS and the middle MS appears to be more concentrated than the red MS with a significance level for this result which is above 3σ.

Key words: Hertzsprung – Russell and colour – magnitude diagrams – globular clusters: individual: NGC2808.

1 INTRODUCTION

The massive globular cluster (GC) NGC 2808 is one of the most intriguing objects in the context of multiple stellar populations. The most astonishing feature of its colour–magnitude diagram (CMD) is the presence of five distinct sequences of main sequence (MS), and red giant branch (RGB) stars (Piotto et al. 2007; Milone et al. 2015 – hereafter Paper III; Milone et al. 2012a – hereafter M12) and at least four distinct horizontal-branch (HB) segments (Bedin et al. 2000).

Spectroscopy of bright RGB stars has revealed an extreme chemical composition with extended Na–O (Carretta et al. 2006; Gratton et al. 2013; Marino et al. 2014) and Mg–Al (Carretta 2014) anticorrelations.

The distinct sequences in the CMD of NGC 2808 correspond to multiple stellar populations with light element abundance variations and different helium content. In particular, the three most evident MSs discovered by Piotto et al. (2007), namely red, middle, and blue MS (rMS, mMS, and bMS) have been interpreted with three stellar populations with primordial helium abundance ($Y \sim 0.25$) and with extreme values of $Y \sim 0.32$, $Y \sim 0.38$ (D'Antona & Caloi 2004; D'Antona et al. 2005; Piotto et al. 2007; Paper III). Large helium enhancement has been also inferred from spectroscopy of HB stars (Marino et al. 2014) and by the analysis of chromospheric lines in spectra of RGB stars (Pasquini et al. 2011).

The formation and evolution of stellar populations in GCs have been widely investigated by several authors (see e.g. Renzini et al. 2015 and references therein). The fraction of stars in each population, their radial distribution, chemical composition, mass function, and dynamics are amongst the diagnostics commonly used to constraint the various scenarios. In particular, the radial distribution of stellar populations can provide information on the series of events that led from massive clouds in the early Universe to the present day GCs with their multiple stellar populations. Indeed clusters with long relaxation times may still keep information of the initial conditions of their stellar populations.

Theoretical models and simulations by D'Ercole et al. (2008, 2010) predict that stars enhanced in helium and sodium are more centrally concentrated than stellar populations with primordial

★ E-mail: msimioni@iac.es

Table 1. List of the used *HST* images. The average radial distance from the clusters centre, *R*, is indicated for each field.

GO	PI	Camera	Filter	Exposures	*R*	Epoch
9899	G. Piotto	WFC/ACS	*F*475*W*	6 × 340 s	3.34 arcmin	05 May 2004
10775	A. Sarajedini	WFC/ACS	*F*814*W*	23 s +5 × 370 s		01 Jan 2006
10922	G. Piotto	WFC/ACS	*F*475*W*	2 × 350s	3.40 arcmin	09 Aug 2006
				2 × 360 s	3.38 arcmin	01 Nov 2006
			*F*814*W*	3 × 350 s	3.40 arcmin	09 Aug 2006
				3 × 360 s	3.38 arcmin	01 Nov 2006
12605	G. Piotto	WFC/ACS	*F*475*W*	6 × 890 s +6 × 982 s	6.27 arcmin	08 Sept 2013
			*F*814*W*	6 × 508 s	6.27 arcmin	08–09 Sept 2013
12605	G. Piotto	UVIS/WFC3	*F*275*W*	12 × 985 s		08–09 Sept 2013

helium and oxygen abundance. This scenario is in agreement with observational studies on some GCs (e.g. 47Tuc and ωCen, Sollima et al. 2007; Bellini et al. 2009; NGC 3201, Carretta et al. 2010; M2, M3, M5, M13, M15, M53, M92, Lardo et al. 2011; Milone et al. 2012b; NGC 2419, Beccari et al. 2013; NGC6388 and NGC6441, Bellini et al. 2013; NGC 362, Carretta et al. 2013; Cordero et al. 2014) while in other cases the multiple stellar populations share the same radial distribution (e.g. NGC 1851, NGC 6121 (M4), NGC 6362, and NGC 6752, see Milone et al. 2009a; Dalessandro et al. 2014; Nardiello et al. 2015).

In this paper, we exploit proprietary data from the Wide Field Channel of the Advanced Camera for Surveys (WFC/ACS) and the Ultraviolet and Visual Channel of the Wide Field Camera III (UVIS/WFC3) to investigate for the first time the radial distribution of the multiple MSs in NGC 2808. We also show the results of a simple *N*-body simulations aimed at illustrating and providing some insight on the possible spatial mixing and dynamical history of this cluster. This paper is part of the *Hubble Space Telescope* (*HST*) UV Legacy Survey of Galactic GCs that is a project to investigate 57 Galactic GCs through the filters *F*275*W*, *F*336*W,* and *F*438*W* of UVIS/WFC3 (GO-13297, PI. G. Piotto, see Piotto et al. 2015 – hereafter Paper I – for details). The paper is organized as follows: in Section 2, we present the data and the data analysis; Section 3 describes in detail the methods used to derive the fraction of bMS, mMS, and rMS stars and the simulation performed for the theoretical analysis. Results are then presented in Section 4, and discussed in Section 5.

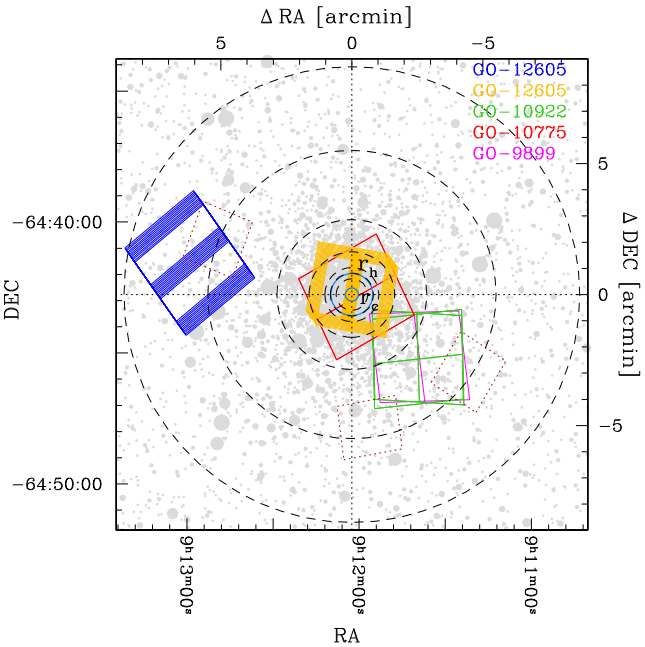

Figure 1. Finding chart for the used images. Core and half-light radii of NGC 2808 (r_c = 0.25 arcmin and r_h = 0.80 arcmin, Harris 1996, 2010 edition) are indicated by cyan circles. For each used set, the corresponding footprints are shown: red-dotted fields corresponds to WFC3 IR observations of GO-11665. Dashed circles represent the boundaries of the selected radial bins; see text for details.

2 DATA AND DATA ANALYSIS

In order to study the radial distribution of the multiple MSs and RGBs of NGC 2808, we have exploited the data set listed in Table 1 which consists of images taken with ACS/WFC and UVIS/WFC3 on board of *HST*. These data are part of GO-9899, GO-10922, GO-12605 (PI. G. Piotto), and GO-10775 (PI. A. Sarajedini) and most of them have been already used by our group to study multiple stellar populations in this cluster (e.g. Piotto et al. 2007, Paper I; Sarajedini et al. 2007; Anderson et al. 2008a; M12).

The footprints of the data are shown in Fig. 1, where we indicate with different colour codes the images from different GOs. Stars in the most external field have radial distance of $\Delta r \sim 8.5$ arcmin at most and lie approximately halfway from the tidal radius of NGC 2808 which is $r_t = 9.08$ arcmin (Harris 1996, 2010 edition).

We have used the photometric and astrometric catalogues presented by M12 from the GO-9899 and GO-10922 data set, and the catalogue from Anderson et al. (2008a) for GO-10775. The photometric and astrometric reduction for GO-12605 data has been carried out as described below.

We have first corrected the charge-transfer efficiency effects in each image by using the method and the software by Anderson & Bedin (2010).

Photometry and astrometry of ACS/WFC images has been performed as in Anderson et al. (2008a). Briefly, we have used two distinct methods to measure bright and faint stars. To determine flux and position of bright stars, we have analysed each image, independently, by using the point-spread function models from Anderson & King (2006) plus a spatially constant perturbation that accounts for small focus variations due to the 'breathing' of *HST*. The derived magnitudes and positions are then combined. The flux and the position for very faint stars, which cannot be robustly measured in every individual image, have been determined by fitting for each star simultaneously all the pixels in all the exposures (see section 5 of Anderson et al. 2008b for more details). Stellar positions have been corrected for geometrical distortion by using the solution provided by Anderson & King (2006). UVIS/WFC3 images have been analysed similarly. In this case, we derived the PSFs as in Anderson et al. (2006) and Bellini et al. (2010) and used distortion

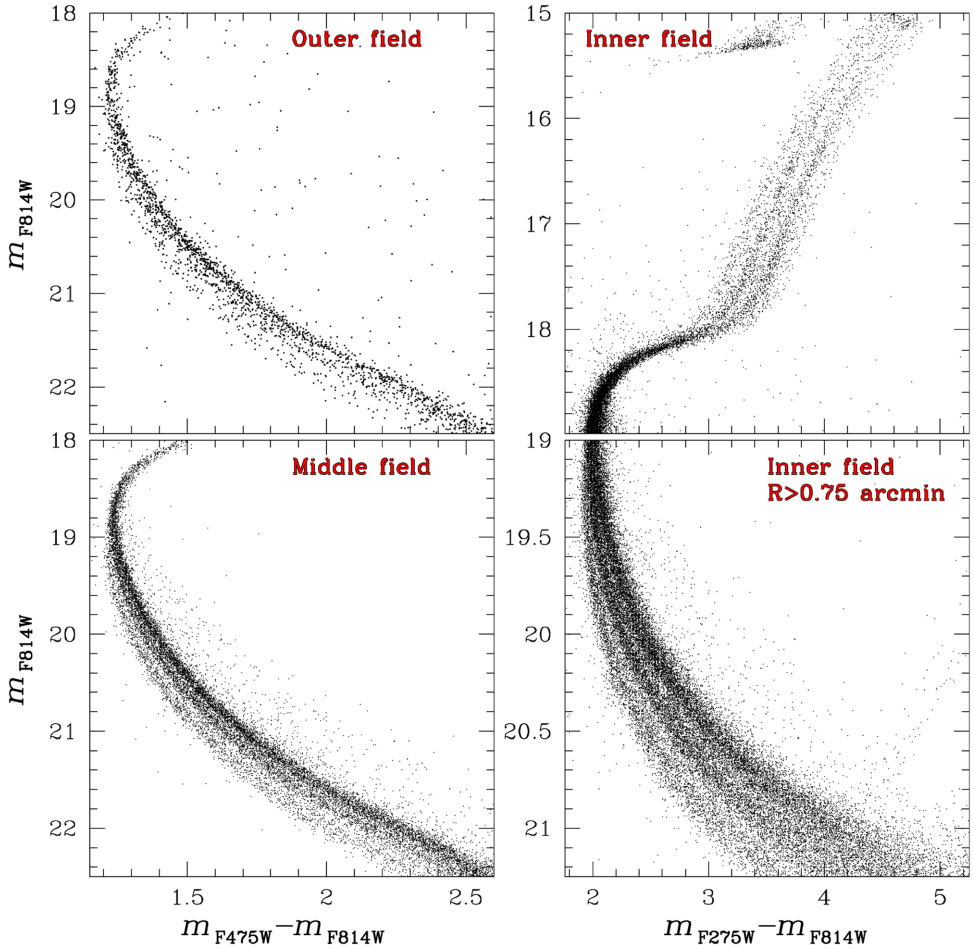

Figure 2. CMDs corrected for differential reddening used to determine the fraction of stars in the multiple MSs of NGC 2808 in the outer and middle field (left-hand panels), and the fraction of multiple MSs and RGBs in the inner field (right-hand panels).

solution by Bellini & Bedin (2009) and Bellini, Anderson & Bedin (2011).

We have used the several indexes provided by the software as diagnostics of the quality of photometry (Anderson et al. 2008a). Since high-accuracy photometry is required to analyse the multiple MSs and RGBs in NGC 2808, we have adopted the method described by Milone et al. (2009b) and Bedin et al. (2009) to select a sub-sample of stars that have small astrometric errors, are relatively isolated, and well fitted by the PSF as in Milone et al. (2009b, Section 2.1).

Photometry has been calibrated as in Bedin et al. (2005). For the WFC/ACS images, we used the zero-points provided by Bedin and collaborators, while for UVIS/WFC3 we adopted the zero-points listed in the Space Telescope Science Institute (STScI) web page for WFC/ACS and WFC3/UVIS.[1] Each CMD has been corrected for differential reddening as in M12.

The CMDs used to study the radial gradient of multiple populations in NGC 2808 are shown in Fig. 2. For the central and middle field where stellar proper motions were available from Piotto et al. (2007) and Paper III we analysed only stars that according to their motion are cluster members (see Piotto et al. 2007 for details). On the contrary, there are no proper motions for stars in the outer field and we will account for field-star contamination by using the Galactic model from Girardi et al. (2005) as discussed in Section 3. In the outer and middle field, we have analysed the m_{F814W} versus $m_{F475W} - m_{F814W}$ CMD and studied multiple populations in the magnitude interval $19.50 < m_{F814W} < 22.00$, where the three MSs are clearly visible. In the inner field, we analysed MS stars with $19.50 < m_{F814W} < 21.25$ and limited our study to the region with distance from the cluster centre, $R > 0.75$ arcmin, indeed crowding prevents us to clearly distinguish the triple MS at smaller radii. In this case, we used the m_{F814W} versus $m_{F275W} - m_{F814W}$ CMD. Furthermore, we analyse the radial distribution of multiple populations along the RGB in the entire inner field.

2.1 Artificial stars

The artificial-star (AS) experiments have been performed as in Anderson et al. (2008a). We have generated a list of 300 000 stars and placed them along each MS and RGB of NGC 2808 by assuming the same spatial distribution as observed for real stars (see M12 for details).

For each star in the input list, we have generated a star in each image, and measures it by using the same procedure as for real stars. We assumed an AS as found when the input and the output position differ by less than 0.5 pixel and the input and the output flux by less than 0.75 mag. Finally, we have selected a sub-sample

[1] http://www.stsci.edu/hst/wfc3/phot_zp_lbn; http://www.stsci.edu/hst/acs/analysis/zeropoints/zpt.py

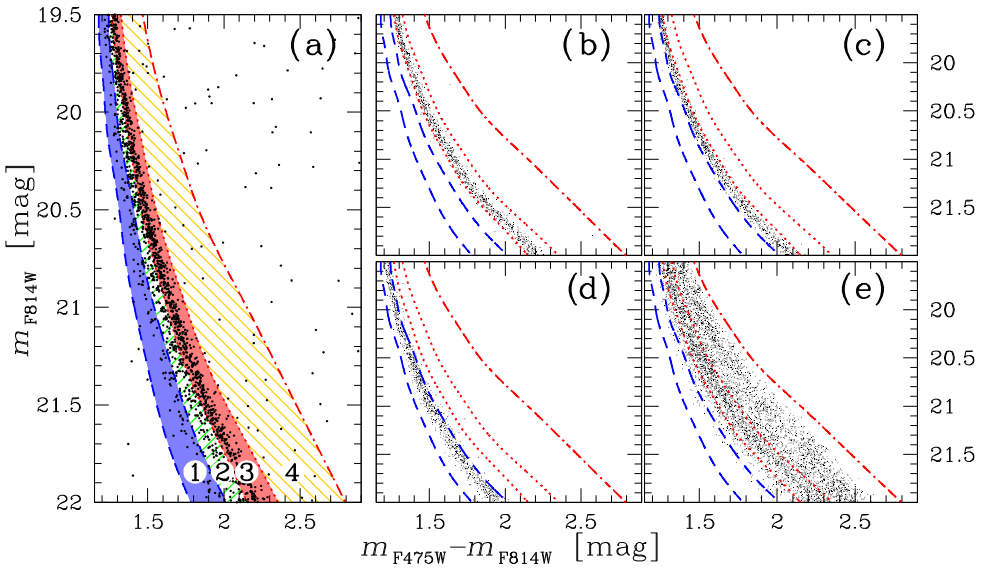

Figure 3. Method used to determine the fraction of bMS, mMS, and rMS stars and the fraction of binaries from GO-12625 ACS/WFC data. Blue-dashed and red-dotted lines have been obtained by shifting the fiducials of the bMS and the rMS by $\pm 3\sigma_{\rm bMS}$ and $\pm 3\sigma_{\rm rMS}$, respectively. The red-dash–dotted line plotted in each panel is the fiducial line of equal-mass binaries redshifted by $3\sigma_{\rm rMS}$. These lines are the boundaries of four regions, R_1–R_4 of the CMD coloured blue, green, red, and yellow, respectively, in panel (a). The observed CMD for NGC 2808 stars is plotted in panel (a), while panels (b), (c), and (d) show the simulated CMD for single rMS, mMS, and bMS stars, respectively. The CMD of panel (e) is made only of MS–MS binaries (see text for details).

of relatively isolated ASs with small astrometric errors, and well fitted by the PSF by using the same procedure as for real stars indeed the software by Anderson et al. (2008a) provides for ASs the same diagnostics of the photometric quality as for real star.

ASs have been used to estimate errors of the photometry used in this paper and the completeness level. Completeness have been derived for each star as in M12.

3 THE FRACTION OF STARS IN THE THREE MSs

To compare the radial distribution of each stellar population and highlight the presence of gradients among them, the number of stars in each MS has been counted. These values have been thus normalized to the total number of MS stars observed in the analysed magnitude ranges in order to obtain the so-called population ratio. To derive the number of stars in each MS ($N_{\rm bMS}$, $N_{\rm mMS}$, and $N_{\rm rMS}$) and the fraction of binaries ($f^{\rm BIN}$) in each field of NGC 2808, we adopted the iterative procedure introduced by M12 and illustrated in Fig. 3 for the CMD of the outer field. The blue-dashed lines and the red-dotted lines plotted in each panel of Fig. 3 are obtained by shifting by plus or minus $3\sigma_{\rm bMS}$ and $3\sigma_{\rm rMS}$ the fiducial line of rMS and bMS, respectively. The red dash–dotted line is the fiducial line of equal mass rMS–rMS binaries redshifted by $3\sigma_{\rm rMS}$. The fiducials and the corresponding errors have been determined as in M12.

These lines are the boundaries of four regions that we name R_1, R_2, R_3, and R_4 and coloured blue, green, red, and yellow, respectively. The majority of the bMS, mMS, and rMS stars are located in the regions R_1, R_2, and R_3, while the region R_4 is mostly populated by MS–MS binaries. As discussed by M12, a fraction of bMS also migrates into regions $R_{2,3,4}$, and similar shift applies to some mMS and rMS stars. Moreover regions R_1, R_2, and R_3 are also populated by MS–MS binaries.

Specifically, each region R_i is populated by a fraction $f_i^{\rm bMS(mMS,rMS)}$ of bMS (mMS, rMS) stars and a fraction $f_i^{\rm BIN}$ of binaries. The relations between the observed total numbers of stars and the number of stars in each sequence can be expressed, for $i = 1, 2, 3, 4$ as

$$N_i = N_{\rm bMS} f_i^{\rm bMS} + N_{\rm mMS} f_i^{\rm mMS} + N_{\rm rMS} f_i^{\rm rMS} + f^{\rm BIN} N_{\rm MS} f_i^{\rm BIN}, \quad (1)$$

where $N_{\rm MS}$ is the total number of MS stars. N_i is the number of cluster stars in each region corrected for completeness. In the inner and middle field, where stellar proper motions are available, we have determined N_i from counts of stars that, according to their proper motions, are cluster members. In the outer field, where we do not have proper motions, we have used the Galactic model by Girardi et al. (2005) and estimated the number of cluster stars in each region as $N_i = N_i^{\rm obs} - N_i^{\rm field}$, where $N_i^{\rm obs}$ is the number of stars observed in each region and corrected for completeness, and $N_i^{\rm field}$ is the number of field stars predicted by the Galactic model in the same direction of NGC 2808 and in a field of view with the same area as the outer field.

Since the number of binaries strongly depends on the number of stars in each sequence, and vice versa, in order to derive the unknowns of equation (1) we applied an iterative procedure. We started by assuming a null binary fraction and determine a crude estimate of $N_{\rm bMS}$, $N_{\rm mMS}$, and $N_{\rm rMS}$ by solving the system of equation (1) for $i = 1, 2, 3$.

These numbers have been then used to determine $f_i^{\rm BIN}$. To do this we have generated a CMD made of pure binaries as in M12 by using a flat mass-ratio distribution and assuming that the binary components belong to any of the MSs. The fraction of binaries, $f_i^{\rm bMS(mMS,rMS)}$, in each region R_i, has been determined by computing the ratio between the total number of inserted binaries and the number of binaries in each region. We refer the reader to M12 (see their sections 5.2 and 5.3) for details.

At this stage, we have obtained a raw estimate of $f_i^{\rm BIN}$ and calculated $f_i^{\rm bMS}$, $f_i^{\rm mMS}$, and $f_i^{\rm rMS}$. So we can derive $f^{\rm BIN}$ from equation (1). This ends one iteration.

The values of $N_{\rm bMS}$, $N_{\rm mMS}$, $N_{\rm rMS}$, and $f^{\rm BIN}$ are used to simulate a new CMD, improve the estimate of $f_i^{\rm BIN}$, and again solve the system of equation (1) for $N_{\rm bMS}$, $N_{\rm mMS}$, $N_{\rm rMS}$, and $f^{\rm BIN}$. Following M12, we

Table 2. Fraction of stars in the three main stellar populations of NGC 2808 derived from multiple MSs and RGBs in the three fields analysed in this paper. The magnitude interval is also listed. The fraction of rMS, mMS, and bMS stars determined as described in Section 3 and the fraction of stars of RGB-(A+B+C), RGB-D, and RGB-E from Paper III are listed in the six upper lines of the table. The corresponding fraction of RGB stars inferred from method I are provided at line seven. The last four lines of the table list the population ratios derived from method II. See text for details.

Field	Sequence	m_{F814W} interval	Population ratio rMS or RGB-(A+B+C)	Population ratio mMS or RGB-D	Population ratio bMS or RGB-E	Binary fraction
Outer	MS	19.50–21.25	0.63 ± 0.04	0.27 ± 0.04	0.10 ± 0.03	0.03 ± 0.01
		19.50–22.00	0.62 ± 0.04	0.27 ± 0.04	0.11 ± 0.03	0.03 ± 0.01
Middle	MS	19.50–21.25	0.62 ± 0.02	0.25 ± 0.02	0.13 ± 0.03	0.05 ± 0.01
		19.50–22.00	0.62 ± 0.02	0.24 ± 0.02	0.14 ± 0.03	0.05 ± 0.01
Inner, $R > 0.75$ arcmin	MS	19.50–21.25	0.53 ± 0.02	0.29 ± 0.02	0.18 ± 0.02	0.06 ± 0.01
Inner	RGB	12.40–17.20	0.50 ± 0.03	0.31 ± 0.02	0.19 ± 0.02	–
Inner	RGB	12.40–17.20	0.52 ± 0.03	0.28 ± 0.02	0.20 ± 0.02	–
Outer	MS	19.50–22.00	0.57 ± 0.04	0.30 ± 0.04	0.13 ± 0.03	–
Middle	MS	19.50–22.00	0.57 ± 0.02	0.27 ± 0.02	0.16 ± 0.03	–
Inner, $R > 0.75$ arcmin	MS	19.50–21.25	0.47 ± 0.02	0.32 ± 0.02	0.21 ± 0.02	–
Inner	RGB	12.40–17.20	0.46 ± 0.02	0.33 ± 0.01	0.21 ± 0.01	–

iteratively repeated the procedure until the value $f^{\rm BIN}$ changes by less than 0.001 from one iteration to the successive one.

Each measure is affected by the uncertainties in the determination of the fiducial line and on the corresponding boundaries of the CMD regions R_1–R_4. In order to determine it, we have repeated the procedure described above 1000 times each time by using different fiducials and the boundaries of the four regions, thus determining 1000 values for the population ratio. Each fiducial has been determined by adding to each point of the fiducial a shift in colour, whose value is randomly extracted by a Gaussian distribution with a σ equal to the observed error. We assumed as the uncertainties in the determination of the fiducial line the 68th percentile of the 1000 determination of the population ratio. This uncertainty has been then added in quadrature to the Poisson uncertainty to determine the error associated with each measure.

In the central field, the three MSs are not distinguishable below $m_{F814W} = 21.25$ so we limited the analysis to the $F814W$ magnitude range [19.5–21.25]. In both the outer and middle field, where deep $F475W$ and $F814W$ photometry is available, we have analysed the interval with $19.5 < m_{F814W} < 22.0$ in close analogy with M12. In order to compare results from different fields in the outer and middle field, we also provide results for the interval [19.5–21.25].

4 RESULTS

The obtained fractions of bMS, mMS, and rMS stars and the fraction of binaries in each field are listed in Table 2. In Fig. 4 we plotted the fraction of b(m,r)MS-stars as a function of the average radial distance from the cluster centre of all the analysed stars.

Unfortunately, as discussed in Section 2, due to stellar crowding, the triple MS is not clearly visible in the very central regions of NGC 2808 and we have no information on the population ratio in the innermost 0.75 arcmin. In order to extend the study of the radial distribution of multiple stellar populations to the central regions, we have exploited the results from Paper III.

In that work, we have analysed multiwavelength photometry of NGC 2808 as part of the UV Legacy Survey of Galactic GCs from GO-13297 and GO-10775. We have separated at least five distinct populations that we name A, B, C, D, and E. The five populations are clearly visible along the RGB in the entire analysed field of view, which corresponds to the inner field analysed in this paper. Specifically, populations D and E correspond to the mMS and the bMS identified by Piotto et al. (2007), while populations A, B, and C are associated with the rMS. The fraction of stars in the five RGBs are $f^{\rm RGB\text{-}A} = 5.8 \pm 0.5$ per cent, $f^{\rm RGB\text{-}B} = 17.4 \pm 0.9$ per cent, $f^{\rm RGB\text{-}C} = 26.4 \pm 1.2$ per cent, $f^{\rm RGB\text{-}D} = 31.3 \pm 1.3$ per cent, and $f^{\rm RGB\text{-}E} = 19.1 \pm 1.0$ per cent of the total number of RGB stars with $12.25 < m_{F814W} < 17.70$, respectively. Therefore, the progeny of the rMS, which corresponds to the RGBs A, B, and C include $f^{\rm RGB\text{-}(A+B+C)} = 49.6 \pm 1.6$ per cent of the total number of MS stars. The interval of luminosity analysed in Paper III for the study of multiple RGBs obviously differs from that of this paper. In order to properly compare RGB and MS stars, we have adopted two different methods.

4.1 Crude estimate (method I)

The first method is based on the comparison of results from multiple MS corresponding to the $F814W$ magnitude bin [19.5–21.25] and from the RGB. Specifically, we have first derived the population ratios from four distinct sample of stars that include MS stars of the inner, middle, and outer field and RGB stars of the inner field.

To compare results from the RGB and the MS, we used the photometric catalogue from Paper III and estimated the fraction of RGB-E, RGB-D, and RGB-(A+B+C) as done in that paper but for stars with radial distance from the cluster centre larger than 0.75 arcmin. This is the same region of the inner field, where we have determined the fraction of bMS, mMS, and rMS stars.

We found that the fraction of RGB-(A+B+C), RGB-D, and RGB-E stars are $f^{\rm RGB\text{-}(A+B+C)}_{\rm inner\ field,\ R>0.'75} = 0.51 \pm 0.03$, $f^{\rm RGB\text{-}D}_{\rm inner\ field, R>0.'75} = 0.32 \pm 0.02$, $f^{\rm RGB\text{-}E}_{\rm inner\ field, R>0.'75} = 0.17 \pm 0.02$. For completeness, we derived the population ratio for stars with radial distance from the cluster centre $R < 0.75$ arcmin. We find $f^{\rm RGB\text{-}(A+B+C)}_{\rm inner\ field, R<0.'75} = 0.49 \pm 0.03$, $f^{\rm RGB\text{-}D}_{\rm inner\ field,\ R<0.'75} = 0.30 \pm 0.02$, $f^{\rm RGB\text{-}E}_{\rm inner\ field,\ R<0.'75} = 0.21 \pm 0.03$ and conclude that there is no evidence for significant difference in the population ratio derived within the region with radial distance $0.00 < R < 0.75$ arcmin and the region with $0.75 < R < 2.10$ arcmin.

We thus imposed the same fraction of stars along the three MSs and the corresponding RGBs in the region of the inner field with

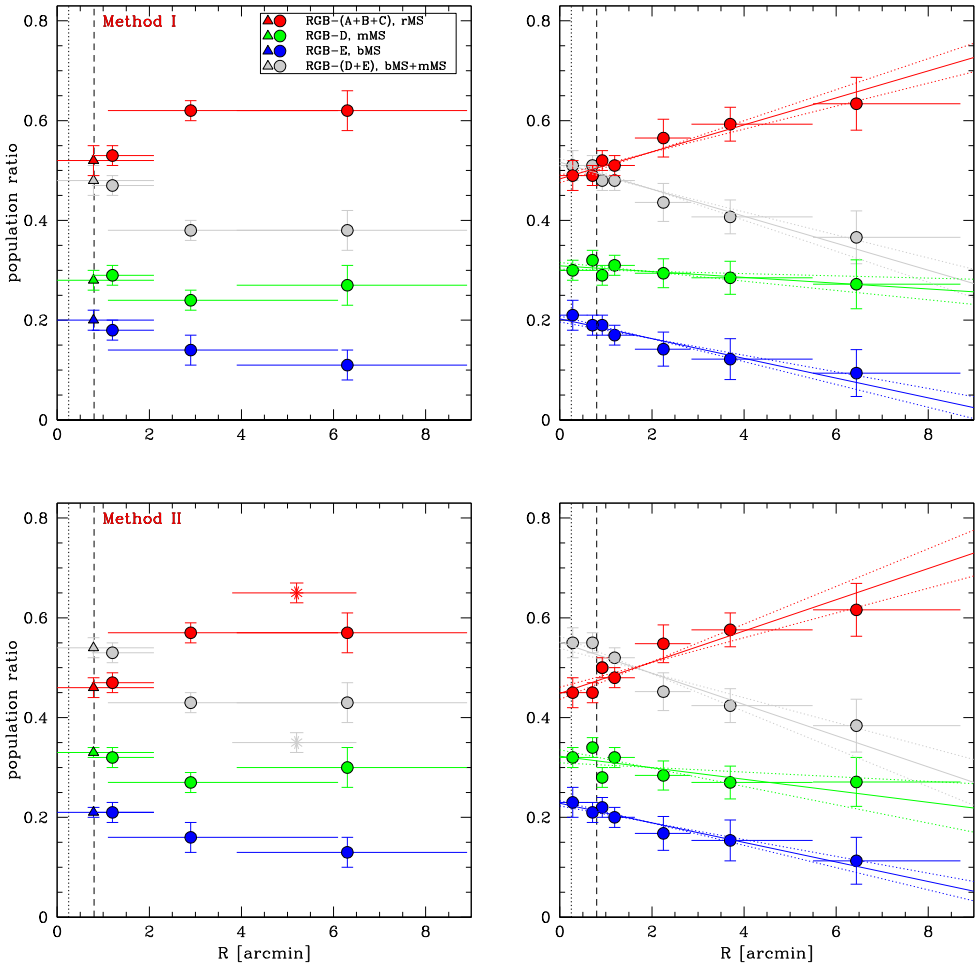

Figure 4. Fraction of bMS (blue symbols), mMS (green symbols), rMS (red symbols), and bMS+mMS (grey symbols) stars respect to the total number of MS stars as a function of the radial distance from the cluster centre. The triangles used in the left-hand panels indicate the values of population ratios inferred from RGB stars, while the squares refer to results from the MS. The red and grey asterisks plotted in the lower-left panel indicate the population ratio inferred by Milone et al. (2012c) in their study of low-mass MS stars. The horizontal lines plotted in each panel span the radial coverage of each bin, while the squares and the triangles indicate the average radial distance of the stars in each region. The vertical dotted and dashed lines mark the core and the half-light radius, respectively. Upper and lower panels show results obtained from method I and method II, respectively. In the upper-left and lower-left panel, we have analysed each field independently, while the upper-right and lower-right panel show the results for seven region with different distance from the cluster centre. The best-fitting straight lines are shown in the right-hand panels, where dotted lines represent the maximum- and minimum-slope straight lines.

$R > 0.75$ arcmin and calculated the number of RGB-(A+B+C) stars as

$$N^{\text{RGB-(A+B+C)}}_{\text{inner field}} = N^{\text{RGB-(A+B+C)}} \frac{f^{\text{rMS}}_{\text{inner field}}}{f^{\text{RGB-(A+B+C)}}_{\text{inner field},R>0.'75}}.$$

We derived $N^{\text{RGB-D(E)}}_{\text{inner-field}}$ similarly. Results are listed in Table 2 and illustrated in the upper-left panel of Fig. 4.

The fraction of stars in each sequence in the middle and the outer field agree within 1σ, where approximately 63 per cent of the entire number of the analysed MS stars in the $F814W$ magnitude interval [19.5–21.25] belong to the rMS. The fraction of rMS stars slightly decreases in the central field to about 53 per cent, where it is similar to the fraction of RGB-(A+B+C). The difference between the fraction of rMS stars in the inner and in the outer field is significant at the 2.5σ-level and similar results are obtained when we compare results from the RGB in the inner field with those from the MS in the outer and middle fields.

In contrast, the fraction of mMS plus bMS stars seems to increase when moving from the cluster outskirts to the centre, and both the bMS and the mMS are more centrally concentrated than the rMS. We note, that one of the main disadvantages of the analysis illustrated in the upper-left panel of Fig. 4 is that, in some cases, distinct fields cover the same radial interval and the large size of each bin has the effect of diluting and hiding in part any existing radial gradient. In order to further explore the radial distribution of the multiple stellar populations in NGC 2808 and better identify the presence and strength of radial gradients, it is necessary to use a finer and non-overlapping binning.

In order to further investigate the radial distribution of multiple stellar populations in NGC 2808, we have divided the stars studied in this paper into seven groups with different radial distance from the cluster centre and calculated the population ratio in each region. Specifically, we have defined a circle with radius $R = 0.60$ arcmin where photometry of RGB stars only is available and three additional regions included in the inner field such that, each region contains the same number of MS stars. Moreover, we have defined three additional annuli that include stars in the middle and the outer field. The boundaries of these seven regions are plotted with dashed circles in Fig. 1. We have verified that the conclusion of the paper

Table 3. Population ratios measured in the redefined radial sampling (see text for details); $R_{\rm min}$, $R_{\rm max}$, and $R_{\rm med}$ are, respectively, the minimum, the maximum, and the median radial distances of the bin. The first seven lines are referred to method I while the lower part is referred to method II.

$R_{\rm min}$ (arcmin)	$R_{\rm max}$ (arcmin)	$R_{\rm med}$ (arcmin)	Population ratio rMS	Population ratio mMS	Population ratio bMS	Population ratio mMS+bMS
0.00	0.60	0.28	0.49 ± 0.03	0.30 ± 0.02	0.21 ± 0.03	0.51 ± 0.036
0.60	0.82	0.71	0.49 ± 0.02	0.32 ± 0.02	0.19 ± 0.02	0.51 ± 0.028
0.82	1.03	0.92	0.52 ± 0.02	0.29 ± 0.02	0.19 ± 0.02	0.48 ± 0.028
1.03	1.63	1.19	0.51 ± 0.02	0.31 ± 0.02	0.17 ± 0.02	0.48 ± 0.028
1.63	2.84	2.25	0.565 ± 0.038	0.294 ± 0.029	0.142 ± 0.034	0.436 ± 0.045
2.86	5.49	3.70	0.593 ± 0.034	0.285 ± 0.033	0.122 ± 0.041	0.407 ± 0.053
5.50	8.70	6.44	0.634 ± 0.053	0.272 ± 0.049	0.094 ± 0.047	0.366 ± 0.068
0.00	0.60	0.28	0.45 ± 0.03	0.32 ± 0.02	0.23 ± 0.03	0.55 ± 0.036
0.60	0.82	0.71	0.45 ± 0.02	0.34 ± 0.02	0.21 ± 0.02	0.55 ± 0.028
0.82	1.03	0.92	0.50 ± 0.02	0.28 ± 0.02	0.22 ± 0.02	0.50 ± 0.028
1.03	1.63	1.19	0.48 ± 0.02	0.32 ± 0.02	0.20 ± 0.02	0.52 ± 0.028
1.63	2.84	2.25	0.548 ± 0.038	0.284 ± 0.029	0.168 ± 0.034	0.452 ± 0.045
2.86	5.49	3.70	0.576 ± 0.034	0.270 ± 0.033	0.154 ± 0.041	0.424 ± 0.053
5.50	8.70	6.44	0.616 ± 0.053	0.271 ± 0.049	0.113 ± 0.047	0.384 ± 0.068

Table 4. Slope and intercept values (a and b, respectively), together with their uncertainties ($\sigma_{\rm a}$ and $\sigma_{\rm b}$), of best-fitting least-squares lines for rMS, mMS, bMS, and mMS+bMS, respectively, referred to method I; see text for details.

sequence	a	$\sigma_{\rm a}$	b	$\sigma_{\rm b}$
rMS	0.027	0.004	0.483	0.007
mMS	− 0.006	0.003	0.309	0.007
bMS	− 0.020	0.003	0.202	0.006
mMS+bMS	− 0.027	0.004	0.517	0.007

does not depend either on the location or on the number of regions that we use to study the radial distribution of multiple stellar populations.

Results are listed in Table 3 and illustrated in the upper-right panel of Fig. 4, where the continuous lines are the best-fitting weighted-least-squares straight lines. The values of the slope a and the intercept b of each line are listed in Table 4 together with the corresponding uncertainties.

The slope corresponding to the rMS is larger than zero with a significance greater than 6σ, while both the blue and the middle exhibit negative values of a with a significance of $\sim 6.5\sigma$ and $\sim 1.5\sigma$, respectively. By assuming a flat distribution, and the same uncertainties as in our population-ratio estimates, 10^6 Monte Carlo simulations indicate that we have a probability of 2×10^{-4} to get a slope equal to or higher than that observed for rMS stars. In the case of the bMS, the probability that the observed gradient is due to measurement errors is 4×10^{-3}.

Comparing rMS, mMS, and bMS, it can be noted that the bMS appears to be the most concentrated, having the minimum slope value among them. The difference between the slopes associated with rMS and bMS results to be significant at 12σ. The mMS is also more concentrated than the rMS with a difference between the two slopes that is significant at $\sim 7\sigma$.

4.2 A more sophisticated estimate (method II)

As a second method to compare results from the RGB and from the MS, we follow the recipe by Milone et al. (2009a,b) in their study of the radial distribution of stellar populations along the subgiant branch of NGC 1851. Sure enough, stars in different intervals of luminosity (like the sample of RGB and MS stars analysed in this paper) have different masses; moreover, stars with different luminosity but different helium abundance have different masses. This second method takes in account this mass difference in order to properly compare the population ratio inferred from the MS and the RGBs. We have to compensate for the fact that the two stellar groups that define the distinct MSs and RGBs span different mass intervals.

Table 5. Stellar masses for the three main populations of NGC 2808 at different luminosities in the $F814W$ band as inferred from BaSTI isochrones.

m_{F814W} (mag)	$M_{\rm rMS}$ ($M_\odot$)	$M_{\rm mMS}$ ($M_\odot$)	$M_{\rm bMS}$ ($M_\odot$)
12.40	0.856	0.739	0.654
17.70	0.847	0.732	0.648
19.50	0.769	0.679	0.610
21.25	0.600	0.537	0.491
22.00	0.529	0.476	0.435

This method allows us to fully exploit information from the entire magnitude interval with $19.5 < m_{F814W} < 22.0$ in the middle and outer field. We have normalized the number of stars in each sequence to the analysed mass interval as

$$N_{\rm b(m,r)MS}/\Delta\mathcal{M}, \text{ where } \Delta\mathcal{M} = \int_{M1,{\rm b(m,r)MS}}^{M2,{\rm b(m,r)MS}} \phi(\mathcal{M}){\rm d}\mathcal{M}.$$

Here, $\phi(\mathcal{M})$ is the adopted mass function, and $M1$, b(m, r)MS and $M2$, b(m, r)MS are the minimum and the maximum stellar mass in the analysed interval of luminosity. We adopted a similar relation to derive the normalized fraction of stars in the RGB-(A+B+C), RGB-D, and RGB-E.

The masses corresponding to different luminosities are listed in Table 5 and are obtained from BaSTI isochrones (Pietrinferni et al. 2004, 2009) by adopting the same values of distance modulus, reddening, age, metallicity, and helium abundance as in M12. We adopted for the mass function $\phi(\mathcal{M}) = M^{\alpha}$, where we used the values of α derived by M12. Results are listed in Table 2 and shown in the lower panels of Fig. 4.

In the lower-left panel, we have considered each field separately. We confirm results obtained by using the method I, with the population corresponding to the rMS, being less centrally concentrated

Table 6. Slope and intercept values (a and b, respectively), together with their uncertainties (σ_a and σ_b), of best-fitting least-squares lines for rMS, mMS, bMS, and mMS+bMS, respectively, referred to method II; see text for details.

Sequence	a	σ_a	b	σ_b
rMS	0.031	0.006	0.449	0.012
mMS	−0.011	0.007	0.322	0.013
bMS	−0.020	0.003	0.228	0.005
mMS+bMS	−0.031	0.006	0.551	0.012

than the stellar populations of NGC 2808 that are highly helium enhanced. In this case, the difference between the fraction of RGB-(A+B+C) stars derived in the central field (∼57 per cent) and the fraction of rMS in the middle and the outer fields (∼46–47 per cent) is significant at the $\sim 4.0\sigma$ and $\sim 2.5\sigma$ level, respectively.

A recent study, based on images taken with the near-infrared (NIR) channel of WFC3 for stars in three fields have investigated multiple sequences of very low mass stars in NGC 2808. The three analysed NIR/WFC3 fields have all radial distance of ∼5.2 arcmin from the centre of NGC 2808 (Milone et al. 2012c; red-dotted fields in Fig. 1). Two MSs are clearly visible in the magnitude interval with $<21.25 < m_{F160W} < 22.50$. The most-populous ones, contains 65 ± 2 per cent of the total number of analysed stars and corresponds to the rMS, while the remaining 35 ± 2 per cent the sequence associated with the bMS and the mMS. The population ratios derived by Milone et al. (2012c) and normalized to the corresponding mass intervals are in agreement with the results from this paper and are represented with red and grey asterisks in the lower-left panel of Fig. 4.

In the lower-right panel of Fig. 4, we show the results for the seven regions with different radial coverage, in close analogy with what we have done in the upper-right panel. The slopes corresponding to the three sequences are listed in Table 6 and confirm the conclusion of Section 4.1. In this case, Monte Carlo simulations provide a probability smaller than 1×10^{-4} to get a slope equal to or higher than that observed for rMS stars, while the probability that the observed gradient for bMS stars is due to measurement errors is 3×10^{-3}. The difference between mMS and rMS slopes is now significant at $\sim 5\sigma$ while the significance level of the difference between bMS and rMS slopes is $\sim 7\sigma$.

4.3 Theoretical interpretation

The results of our observational analysis show that two helium enhanced populations (bMS and mMS) are more centrally concentrated than the rMS population. This result is in general qualitative agreement with the predictions of multiple-population cluster formation models according to which second-generation (2G) stars should form more concentrated than the initial first-generation (1G) population.

Because of the effects of dynamical evolution on the structural properties of the various stellar populations, a direct connection between the current observed properties and those predicted by cluster formation models is not straightforward. The long-term cluster dynamical evolution will gradually weaken the initial radial gradient in the fraction of 2G stars (see e.g. Vesperini et al. 2013) until complete spatial mixing when no memory of the initial differences is preserved and all the populations share the same spatial distribution.

As discussed in the Introduction, a few observational studies have found clusters still retaining memory of the initial differences in the spatial distribution of 1G and 2G populations while others appear to have reached the phase when different populations are completely mixed. For those clusters for which a radial gradient in the fraction of 2G stars is still present, the strength of the current observed radial gradient provides a lower limit on what must have been a stronger initial gradient.

A complete and detailed model for any specific individual cluster is a very challenging and computationally expensive task (see e.g. Giersz & Heggie 2011; Heggie 2014); the presence of multiple populations with the additional complexities related to their formation and dynamical history further complicates this task. This is well beyond the scope of the goals of this paper and is deferred to future investigations. Here, in order to illustrate the process of spatial mixing of multiple stellar populations and provide some initial insight on the possible dynamical history leading to the gradient found in our analysis, we present the results of a simple N-body simulation focusing our attention on the two-body relaxation-driven long-term evolution of the spatial distributions of the 1G and 2G population. We started our simulation with 50 000 particles with the 1G and the 2G populations each having half of the total mass of the system and a range of stellar masses equal to those expected at about 12 Gyr for a system with a Kroupa (2001) stellar initial mass function. Both populations are characterized by a King (1966) density profile with central dimensionless potential $W_0 = 7$, but the 2G population is initially concentrated in the inner regions of the cluster and has a half-mass radius about 4.5 times smaller than that of the 1G population. The simulation was run on the Big Red II supercomputer at Indiana University with the GPU-accelerated version of the NBODY6 code (Aarseth 2003; Nitadori & Aarseth 2012).

The cluster is initially tidally limited and assumed to be on a circular orbit in the external potential of a host galaxy modelled as a point mass. We focus here solely on the long-term evolution driven by two-body relaxation and its effect on the spatial distributions of the two populations (see also Vesperini et al. 2013 for further discussion on the long-term evolution and dynamics of spatial mixing).

In Fig. 5, we show the time evolution of the radial profile of the ratio of the number of 2G to 1G stars for stars with masses between 0.6 and 0.8 $M_\odot$ along with the observed ratios for N_{bMS}/N_{rMS}, N_{mMS}/N_{rMS}, and $N_{bMS+mMS}/N_{rMS}$. The results of the simulations illustrate the progressive weakening of the initial radial gradient. In particular, the radial gradient in the fraction of bMS and mMS stars currently observed in NGC 2808 is approximately consistent with those found in the simulation at times $t/t_{rh}(t) \geq 7$. This figure shows a possible dynamical path and the significantly stronger initial gradient behind the current structural properties of the multiple populations of NGC 2808.

As already discussed in the Introduction, NGC 2808 is a particularly complex cluster; the early dynamics during the sequence of events that led to the formation of the different populations observed in this cluster are still unclear. A more detailed exploration of the possible differences in the early and long-term dynamical evolution of different populations and the implications for the current observed properties will require a much more extensive study than that presented here.

5 SUMMARY AND CONLUSIONS

NGC 2808 is one of the most-massive GCs in the Galaxy and hosts at least five distinct stellar populations, namely A, B, C, D, and E, with different content of helium and light elements (Paper III). Populations D and E are highly enhanced in helium up to $Y \sim 0.32$ and ∼0.38 and correspond to the mMS and the bMS discovered

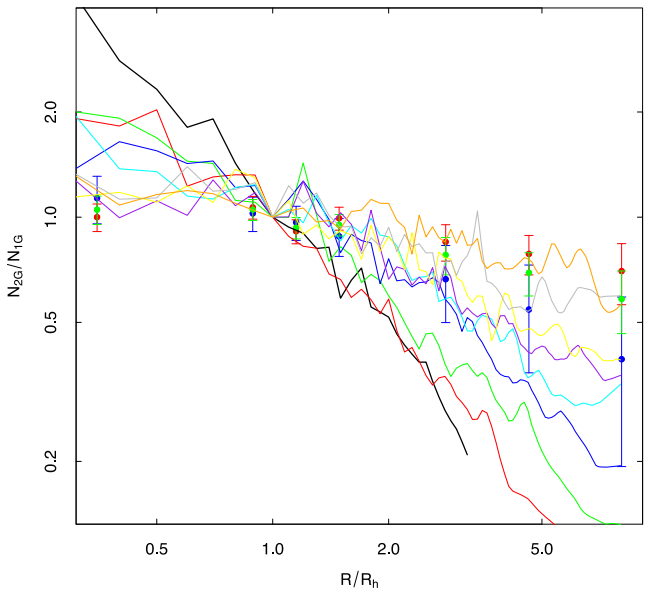

Figure 5. Time evolution of the radial profile of the ratio of the number of 2G to 1G stars (normalized to the value measured at the half-mass radius) versus the projected distance from the cluster centre (normalized to the half-mass radius) for the simulation discussed in the paper (see Section 4.3). Different curves correspond to the profiles measured at values of $t/t_{\rm rh}(t)$ equal to about 0.0 (black line), 2.0 (red line), 3.0 (green line), 5.0 (blue line), 7.0 (cyan line), 8.5 (purple line), 10.3 (yellow line),12.5 (grey line), and 15.3 (orange line). Each radial profile has been calculated by using nine snapshots around the indicated time. Points with error bars show the observed ratio of the number of bMS to rMS stars (blue points), mMS stars to rMS stars (red points) and (bMS+mMS) to rMS stars (green points).

by Piotto et al. (2007). Populations A, B, and C are connected with the red MS by Piotto et al. (2007) and have almost primordial helium abundance. In this paper, we have used both archive and proprietary data collected with the ACS/WFC and WFC3/UVIS on board of *HST* to investigate the radial distribution of the three main populations of NGC 2808 which correspond to the bMS, the mMS, and the rMS. Our data set includes three fields spanning a radial interval that ranges from the cluster centre to approximately 8.5 arcmin.

Parallel ACS@HST observations taken as part of GO-12605 are presented here for the first time (see upper-left panel of Fig. 2 for the obtained CMD). The three MSs have been detected in all the analysed fields. The fraction of stars in each MS has been determined starting from a radial distance of 0.75 arcmin from the cluster centre to 8.5 arcmin. At radial distance smaller than 0.75 arcmin, the three MS cannot be clearly distinguished due to stellar crowding. We have used the photometry of RGB stars from Paper III to extend the study of multiple stellar populations to the cluster centre. Using two different methods, we found that the populations which correspond to the rMS are less centrally concentrated than the helium-rich stellar populations, with a significance for the result that is higher than 3σ. We have also presented the results of a simple *N*-body simulation illustrating the possible evolution of the multiple population spatial mixing of this cluster.

NGC 2808 has a very extended HB which is well populated on both sides of the RR Lyrae instability strip (Sosin et al. 1997). The red HB of NGC 2808 shares the same chemical composition as the stellar populations corresponding to the rMS stars (Gratton et al. 2013; Marino et al. 2014). The bMS corresponds to the bluest HB tail, while the remaining blue-HB stars are connected with the mMS (e.g. D'Antona et al. 2005; Piotto et al. 2007; Dalessandro et al. 2011). Bedin et al. (2000) have investigated the radial distribution of the HB components and find no evidence for a significant gradient. Iannicola et al. (2009) further analysed the radial distribution of HB stars in NGC 2808 and suggested that red-HB stars are less centrally concentrated than the remaining HB stars; although their conclusion is significant only at 1.5σ level, it suggests the presence of a gradient consistent with that we find in our analysis.

Recent studies have investigated the properties of the triple MS in NGC 2808, like the luminosity and mass function and the internal kinematics. M12 have studied the mass functions of the three MSs discovered by Piotto et al. (2007) and found that the slope of rMS-, mMS-, and bMS-mass function are $\alpha = -1.2 \pm 0.3$, $\alpha = -0.9 \pm 0.3$, and $\alpha = -0.9 \pm 0.4$, respectively, i.e. are the same within the errors. In a paper from this series, Bellini et al. (2015), have investigated the internal kinematics of the stellar populations in NGC 2808 by using the same data set from the central field used in this paper. They have found that in the most-external region that they have analysed, between 1.5 and ∼2.0 times the half-light radius, the proper-motion distributions of the populations D and E, are significantly more anisotropic than that of the populations A, B, and C. On the basis of results from *N*-body simulation, Bellini and collaborators have suggested that the kinematic difference between the populations highly enhanced in helium and those with almost primordial helium, are consistent with a scenario, where populations D and E were more-centrally concentrated at the time of their formation.

ACKNOWLEDGEMENTS

This work is based on observations with the NASA/ESA *Hubble Space Telescope*, obtained at the Space Telescope Science Institute, which is operated by AURA, Inc., under NASA contract NAS 5-26555. We thank the anonymous referee for her/his comments that improved the quality of this work. MS, AA, and GP acknowledge support from the Spanish Ministry of Economy and Competitiveness (MINECO) under grant AYA2013-42781. MS and AA acknowledge support from the Instituto de Astrofísica de Canarias (IAC) under grant 309403. GP acknowledges partial support by the Università degli Studi di Padova Progetto di Ateneo CPDA141214 'Towards understanding complex star formation in Galactic globular clusters' and by INAF under the programme PRIN-INAF2014. EV and JH acknowledge support from STScI grant GO-13297.

REFERENCES

Aarseth S. J., 2003, Gravitational N-Body Simulations. Cambridge Univ. Press, Cambridge
Anderson J., Bedin L. R., 2010, PASP, 122, 1035
Anderson J., King I. R., 2006, Instrument Science Report ACS 2006-01, p. 34
Anderson J., Bedin L. R., Piotto G., Yadav R. S., Bellini A., 2006, A&A, 454, 1029
Anderson J. et al., 2008a, AJ, 135, 2055
Anderson J. et al., 2008b, AJ, 135, 2114
Beccari G., Bellazzini M., Lardo C., Bragaglia A., Carretta E., Dalessandro E., Mucciarelli A., Pancino E., 2013, MNRAS, 431, 1995
Bedin L. R., Piotto G., Zoccali M., Stetson P. B., Saviane I., Cassisi S., Bono G., 2000, A&A, 363, 159
Bedin L. R., Cassisi S., Castelli F., Piotto G., Anderson J., Salaris M., Momany Y., Pietrinferni A., 2005, MNRAS, 357, 1038
Bedin L. R., Salaris M., Piotto G., Anderson J., King I. R., Cassisi S., 2009, ApJ, 697, 965
Bellini A., Bedin L. R., 2009, PASP, 121, 1419

Bellini A., Piotto G., Bedin L. R., King I. R., Anderson J., Milone A. P., Momany Y., 2009, A&A, 507, 1393
Bellini A., Bedin L. R., Piotto G., Milone A. P., Marino A. F., Villanova S., 2010, AJ, 140, 631
Bellini A., Anderson J., Bedin L. R., 2011, PASP, 123, 622
Bellini A. et al., 2013, ApJ, 765, 32
Bellini A. et al., 2015, ApJ, 810, L13
Carretta E., 2014, ApJ, 795, L28
Carretta E., Bragaglia A., Gratton R. G., Leone F., Recio-Blanco A., Lucatello S., 2006, A&A, 450, 523
Carretta E., Bragaglia A., D'Orazi V., Lucatello S., Gratton R. G., 2010, A&A, 519, A71
Carretta E. et al., 2013, A&A, 557, A138
Cordero M. J., Pilachowski C. A., Johnson C. I., McDonald I., Zijlstra A. A., Simmerer J., 2014, ApJ, 780, 94
D'Antona F., Caloi V., 2004, ApJ, 611, 871
D'Antona F., Bellazzini M., Caloi V., Pecci F. F., Galleti S., Rood R. T., 2005, ApJ, 631, 868
D'Ercole A., Vesperini E., D'Antona F., McMillan S. L. W., Recchi S., 2008, MNRAS, 391, 825
D'Ercole A., D'Antona F., Ventura P., Vesperini E., McMillan S. L. W., 2010, MNRAS, 407, 854
Dalessandro E., Salaris M., Ferraro F. R., Cassisi S., Lanzoni B., Rood R. T., Fusi Pecci F., Sabbi E., 2011, MNRAS, 410, 694
Dalessandro E. et al., 2014, ApJ, 791, L4
Giersz M., Heggie D. C., 2011, MNRAS, 410, 2698
Girardi L., Groenewegen M. A. T., Hatziminaoglou E., da Costa L., 2005, A&A, 436, 895
Gratton R. G. et al., 2013, A&A, 549, A41
Harris W. E., 1996, AJ, 112, 1487
Heggie D. C., 2014, MNRAS, 445, 3435
Iannicola G. et al., 2009, ApJ, 696, L120
King I. R., 1966, AJ, 71, 64
Kroupa P., 2001, MNRAS, 322, 231
Lardo C., Bellazzini M., Pancino E., Carretta E., Bragaglia A., Dalessandro E., 2011, A&A, 525, A114
Marino A. F. et al., 2014, MNRAS, 437, 1609
Milone A. P., Stetson P. B., Piotto G., Bedin L. R., Anderson J., Cassisi S., Salaris M., 2009a, A&A, 503, 755
Milone A. P., Bedin L. R., Piotto G., Anderson J., 2009b, A&A, 497, 755
Milone A. P., Piotto G., Bedin L. R., Cassisi S., Anderson J., Marino A. F., Pietrinferni A., Aparicio A., 2012a, A&A, 537, A77 (M12)
Milone A. P. et al., 2012b, ApJ, 744, 58
Milone A. P. et al., 2012c, ApJ, 754, L34
Milone A. P. et al., 2015, ApJ, 808, 51 (Paper III)
Nardiello D., Milone A. P., Piotto G., Marino A. F., Bellini A., Cassisi S., 2015, A&A, 573, A70
Nitadori K., Aarseth S. J., 2012, MNRAS, 424, 545
Pasquini L., Mauas P., Kaufl H. U., Cacciari C., 2011, A&A. 531, 35
Pietrinferni A., Cassisi S., Salaris M., Castelli F., 2004, ApJ, 612, 168
Pietrinferni A., Cassisi S., Salaris M., Percival S., Ferguson J. W., 2009, ApJ, 697, 275
Piotto G. et al., 2007, ApJ, 661, L53
Piotto G. et al., 2015, AJ, 149, 91 (Paper I)
Renzini A. et al., 2015, MNRAS, 454, 4197
Sarajedini A. et al., 2007, AJ, 133, 1658
Sollima A., Ferraro F. R., Bellazzini M., Origlia L., Straniero O., Pancino E., 2007, ApJ, 654, 915
Sosin C. et al., 1997, ApJ, 480, L35
Vesperini E., McMillan S. L. W., D'Antona F., D'Ercole A., 2013, MNRAS, 429, 1913

This paper has been typeset from a TEX/LATEX file prepared by the author.